From Self-Organized Criticality to Cosmological Anomalies (Extended Version)

E. Goldfain[1]

[1]Global Institute for Research, Education and Scholarship (GIRES), USA

Abstract

A growing body of observational evidence – the anomalously early appearance of massive galaxies and quasars in JWST deep fields, the cusp-core and missing-satellites problems, the too-big-to-fail problem, and the persistent S_8 tension between weak-lensing and CMB-inferred clustering amplitudes – suggests that structure formation may depart from the scale-independent-gravity assumption of the standard ΛCDM paradigm. This paper develops, in extended form, the proposal that these apparently unrelated anomalies are different observational manifestations of a single dynamical principle: the emergence of Self-Organized Criticality (SOC) in cosmic structure formation, driven by dimensional flow of an underlying multifractal spacetime. We formulate the multifractal measure and its associated generalized (Rényi) dimensions, derive an explicit renormalization-group (RG) trajectory for the anomalous scaling exponent $\epsilon(k)$ from an entropy-extremization principle, and show that the resulting scale-dependent Newton coupling $G_{\text{eff}}(k) = G_0\,[1 + \epsilon(k)]$ modifies the linear growth equation, the spherical-collapse dynamics, the virial theorem, and the halo mass function in a mutually consistent way. We further propose a Landau–Ginzburg free-energy functional whose minimization reproduces the RG flow, place the framework in relation to other approaches exhibiting dimensional flow (Asymptotic Safety, Causal Dynamical Triangulations, multifractional spacetime), and implement a six-module numerical pipeline – background, linear perturbations, matter power spectrum, halo collapse, halo mass function, and weak lensing – that solves the governing equations directly rather than relying on phenomenological parametrizations. Using fiducial parameters, we present illustrative but fully computed predictions for the growth factor, growth index, matter power spectrum, Sheth–Tormen halo mass function, and weak-lensing convergence spectrum, and discuss the sense in which they can, in principle, resolve the anomalies listed above without additional dark-sector physics. This Extended Version supersedes and elaborates upon the shorter companion paper, Goldfain (2026), providing the full derivations, an explicit numerical implementation, and an expanded discussion of observational consequences and theoretical limitations.

Keywords: self-organized criticality, multifractal spacetime, dimensional flow, cosmological anomalies, JWST, cusp-core problem, missing satellites, weak lensing, S_8 tension

Contents

1 Introduction

1.1 The successes and emerging tensions of the standard cosmological model

The concordance ΛCDM cosmological model, built upon General Relativity, cold dark matter, and a cosmological constant, remains the most successful quantitative description of the large-scale Universe. It reproduces the acoustic peaks of the cosmic microwave background (CMB), the baryon acoustic oscillation (BAO) scale, the expansion history inferred from Type Ia supernovae, and the statistics of galaxy clustering over hundreds of megaparsecs (Planck Collaboration, 2020; Weinberg, 2008; Dodelson & Schmidt, 2020). This agreement, spanning more than ten orders of magnitude in physical scale, is one of the principal achievements of twentieth- and twenty-first-century physics.

Despite these successes, the last decade has produced a growing list of discrepancies concentrated precisely at the transition between the linear and nonlinear regimes of gravitational clustering. Individually, each has traditionally been treated as an isolated puzzle requiring its own explanation. Collectively, they raise the possibility that an important physical ingredient is still missing from the standard framework. The most widely discussed tensions include:

- the unexpectedly early appearance of massive, evolved galaxies at redshifts $z \gtrsim 10$ in JWST deep fields (JADES, CEERS, GLASS, COSMOS-Web) (Labbé et al., 2023; Finkelstein et al., 2023; Naidu et al., 2022);
- the discovery of supermassive black holes with $M_{\rm BH} \gtrsim 10^9\,M_\odot$ less than one billion years after the Big Bang (Bañados et al., 2018; Wang et al., 2021);
- the cusp-core discrepancy between simulated Navarro–Frenk–White (NFW) halo profiles and the near-constant-density cores inferred for dwarf and low-surface-brightness galaxies (Navarro et al., 1997; de Blok, 2010);
- the missing-satellites problem (Klypin et al., 1999; Moore et al., 1999);
- the too-big-to-fail problem (Boylan-Kolchin et al., 2011);
- persistent tension between weak-lensing measurements of $S_8 \equiv \sigma_8\sqrt{\Omega_m/0.3}$ and the Planck-derived value under ΛCDM (Heymans et al., 2021; Asgari et al., 2021; DES Collaboration, 2022);
- indications that galaxy assembly at $z \gtrsim 6$ proceeds more rapidly than predicted by conventional hierarchical growth (Boylan-Kolchin, 2023).

None of these tensions individually falsifies ΛCDM; each admits an ad hoc phenomenological cure (baryonic feedback, warm or self-interacting dark matter, revised stellar population synthesis, modified gravity). But their simultaneous appearance, always in the regime where nonlinear gravitational clustering and small-scale structure formation dominate, motivates a re-examination of one of the model's central assumptions: that the effective strength of gravity governing structure formation is independent of the observational scale.

1.2 Cosmological anomalies as a collective phenomenon

An instructive analogy is furnished by condensed-matter physics. Magnetization, superconductivity, and critical opalescence appear superficially unrelated, yet all are now understood as manifestations of universal critical behavior near continuous phase transitions, governed by scale invariance and renormalization-group (RG) flow (Wilson & Kogut, 1974; Cardy, 1996). We pursue the analogous hypothesis that the cosmological anomalies listed above are different observational manifestations of a single critical phenomenon operating during nonlinear cosmic structure formation, in the spirit of our earlier work on continuous-dimension criticality and dimensional flow (Goldfain, 2021, 2022, 2020a,b).

1.3 Gravity as a critical dynamical system

Gravity possesses structural features that favor the emergence of critical behavior. Unlike short-range interactions, Newtonian gravity couples matter over unbounded distances and lacks an intrinsic screening length; combined with the nonlinearity of mode coupling in the growth of density perturbations, this allows self-gravitating systems to evolve through repeated episodes of instability and relaxation without external fine-tuning. These are precisely the ingredients responsible for Self-Organized Criticality (SOC) in driven dissipative systems (Bak et al., 1987, 1988), in which power-law correlations, scale invariance, and intermittent avalanche dynamics emerge dynamically rather than through parameter tuning.

The possibility that cosmic structure formation constitutes an instance of SOC has been raised in various forms over the past three decades (Aschwanden et al., 2016). Previous treatments, however, generally regard criticality as an emergent statistical property of matter clustering, external to the geometry of spacetime itself. The present work instead argues that SOC in cosmic structure formation is the macroscopic dynamical signature of *dimensional flow* in the underlying multifractal geometry of spacetime – i.e., that the critical state is geometric in origin rather than purely statistical.

1.4 Multifractal spacetime and dimensional flow

Several independent approaches to quantum gravity – Causal Dynamical Triangulations (Ambjørn et al., 2005), Asymptotic Safety (Reuter, 1998; Percacci, 2017), Hořava–Lifshitz gravity (Hořava, 2009), Group Field Theory, and multifractional spacetime models (Calcagni, 2010, 2017) – independently suggest that the effective Hausdorff and spectral dimensions of spacetime are not fixed but vary continuously under coarse-graining, approaching their classical values (3+1) only in the deep infrared (IR). We adopt this general concept of dimensional flow while remaining agnostic about its microscopic completion, treating it instead as an effective geometric description of a coarse-grained spacetime that inherits a multifractal measure from primordial complexity (Mandelbrot, 1982; Falconer, 2014; Hentschel & Procaccia, 1983; Halsey et al., 1986).

Within this framework the running of Newton's constant is not introduced as a phenomenological modification of gravity, but emerges as a reparameterization induced by the multifractal geometry: the apparent scale dependence of gravitational strength reflects the changing dimensional support of the gravitational field rather than a new fundamental interaction. This establishes a direct bridge between multifractal spacetime, RG concepts, and the nonlinear dynamics of cosmic structure formation.

1.5 Central hypothesis

The central hypothesis of this paper is:

> *Self-Organized Criticality is the macroscopic dynamical manifestation of dimensional flow in a multifractal spacetime.*

The primordial Universe is assumed to evolve toward a statistically stationary critical state whose geometry is characterized by a scale-dependent Hausdorff dimension $D_H(k)$. The associated dimensional flow generates a running effective gravitational coupling $G_{\rm eff}(k)$ that enhances gravitational growth on large scales while suppressing clustering below a characteristic transition scale k_*. The same mechanism simultaneously modifies halo formation, satellite abundances, density profiles, and the rate of early structure formation – offering a unified account of the anomalies of Sec. 2 without exotic dark-matter particles, finely tuned baryonic feedback, or ad hoc modifications of Einstein's field equations.

1.6 Relation to the Condensed Version and scope of this paper

A condensed presentation of this proposal, restricted to the qualitative argument and the leading-order phenomenology, appeared in Goldfain (2026). The present Extended Version supplies (i) the complete derivation of the multifractal measure and its dimensional flow (Sec. 3); (ii) an explicit entropy-extremization derivation of the RG beta function and an associated Landau–Ginzburg order-parameter description of the critical state (Sec. 4); (iii) the full derivation of the modified linear perturbation equations from the scale-dependent Poisson equation (Sec. 5); (iv) the nonlinear spherical-collapse dynamics, generalized virial theorem, and Sheth–Tormen halo mass function (Sec. 6); (v) a self-contained six-module numerical pipeline that solves these equations directly, rather than relying on the analytic leading-order estimates of the Condensed Version (Sec. 7); and (vi) an expanded comparison with observations, discussion, and appendices containing a first-principles variational sketch of the weak-field limit (Sec. 8–Appendix A).

2 Cosmological Anomalies as Manifestations of a Single Dynamical Principle

2.1 Overview

Table 1 summarizes the anomalies introduced above, their conventional ΛCDM explanations, and the corresponding interpretation within the present SOC/dimensional-flow framework. The unifying feature is that every entry in the table involves the response of gravity to density fluctuations across the transition between large, quasi-linear scales and small, deeply nonlinear scales – precisely the regime in which a scale-dependent coupling $G_{\text{eff}}(k)$ would leave its imprint.

Anomaly	**Standard explanation(s)**	**SOC / dimensional-flow explanation**
Early massive JWST galaxies	Revised stellar populations, top-heavy IMF, bursty star formation	Enhanced large-scale growth, $G_{\text{eff}}/G_0 > 1$ for $k \ll k_*$ (Sec. 5)
Early supermassive black holes	Super-Eddington or direct-collapse seeding	Deeper potential wells at fixed z from enhanced growth (Sec. 6)
Cusp–core problem	Baryonic feedback, SIDM	Softened collapse from $G_{\text{eff}}/G_0 < 1$ at small k-support scales (Sec. 6)
Missing satellites	Warm dark matter, UV photoionization, SN feedback	Suppressed small-scale amplification lowers $\delta n/n$ before star formation acts (Sec. 6)
Too-big-to-fail	SIDM, feedback-driven core formation	Same small-scale suppression mechanism as missing satellites
S_8 tension	Systematics, extended ΛCDM (e.g. evolving dark energy)	Suppressed small-scale power lowers lensing-inferred σ_8 (Sec. 8)

Table 1: Cosmological anomalies and their conventional versus SOC/dimensional-flow interpretations.

2.2 Why one mechanism may explain them all

The anomalies in Table 1 span more than six orders of magnitude in physical scale, from dwarf-galaxy cores to the massive proto-clusters glimpsed by JWST. Despite this diversity, they share four common features: (i) all arise during nonlinear gravitational clustering; (ii) all involve the transition between large and small spatial scales; (iii) all probe the effective strength of gravity rather than the homogeneous cosmological background; (iv) all require modifications to the growth history of density perturbations rather than to the background expansion. These shared features motivate treating the anomalies not as independent problems but as different observational windows onto a single dynamical process.

2.3 Transition to the mathematical framework

The discussion above is deliberately phenomenological. Secs. 3–6 develop the corresponding mathematical framework: starting from a scale-dependent geometric measure (Sec. 3), we derive the dimensional flow of the generalized Hausdorff dimension and the RG trajectory of the associated anomalous exponent (Sec. 4), obtain the scale-dependent gravitational coupling and the modified linear perturbation equations (Sec. 5), and extend the analysis into the nonlinear regime of spherical collapse and halo statistics (Sec. 6).

3 Multifractal Spacetime and Dimensional Flow

3.1 Motivation

Section 2 argued that a broad spectrum of cosmological anomalies may reflect a common dynamical mechanism. To convert this observation into a predictive theory we must identify the geometric origin of the proposed scale dependence of gravity. In classical General Relativity, spacetime is a smooth four-dimensional pseudo-Riemannian manifold with metric $g_{\mu\nu}$ and invariant measure

$$d\mu = \sqrt{-g}\, d^4x. \tag{1}$$

Equation (1) implicitly assumes that the local Hausdorff dimension equals the topological dimension everywhere, $D_H = 4$. As reviewed in Sec. 1, this assumption is challenged by several independent quantum-gravity programs, all of which exhibit some form of dimensional flow toward $D_H = 4$ only in the deep IR.

3.2 Fractal measures

A smooth D-dimensional manifold assigns to a ball of radius R a volume $V(R) \propto R^D$ with D integer. A fractal support instead satisfies

$$V(R) \propto R^{D_H}, \qquad D_H \in \mathbb{R}^+, \tag{2}$$

with generally non-integer D_H that may itself depend on the coarse-graining scale $k \sim 1/R$:

$$D_H = D_H(k). \tag{3}$$

Equation (3) is the central geometric assumption of this work: the Universe is viewed not as a homogeneous continuum but as a hierarchy of continuously evolving effective dimensions.

3.3 Multifractal geometry and generalized dimensions

Observations of cosmic structure show that no single fractal exponent describes matter clustering over all scales simultaneously; galaxy clusters, filaments, and voids coexist with markedly different local scaling. We therefore introduce a family of generalized dimensions D_q defined through the Rényi entropy of the coarse-grained matter distribution (Rényi, 1961, 1970; Hentschel & Procaccia, 1983),

$$S_q(\ell) = \frac{1}{1-q} \ln \left[\sum_i p_i(\ell)^q \right], \qquad D_q \equiv \lim_{\ell \to 0} \frac{S_q(\ell)}{\ln(1/\ell)}, \tag{4}$$

where $p_i(\ell)$ is the fraction of matter contained in the i-th cell of a partition of scale ℓ. Positive q weights dense structures; negative q weights underdense voids. The complete spectrum $\{D_q\}_{q\in\mathbb{R}}$ characterizes the full hierarchy of clustering; for a monofractal, D_q is q-independent, while a genuinely multifractal measure has D_q strictly decreasing in q (Halsey et al., 1986). The correlation dimension D_2, obtained from $q = 2$, controls the two-point correlation function and is the quantity most directly probed by galaxy surveys (Sec. 5).

3.4 Dimensional flow

The scale dependence of the generalized dimensions implies a flow equation

$$k \frac{dD_q}{dk} = \beta_q(D_q), \tag{5}$$

formally analogous to the RG flow of a coupling constant, with D_q playing the role of a running "charge." Near an IR fixed point $D_q \to D_q^{\mathrm{IR}} = 4$ (the classical value), we write

$$D_q(k) = 4 - \epsilon_q(k), \qquad \epsilon_q(k) \to 0 \quad (k \to 0), \tag{6}$$

where $\epsilon_q(k)$ is a small anomalous dimension, analogous to the anomalous dimensions of conventional RG theory but here associated with the coarse-graining of a geometric, rather than a field-theoretic, measure. Unlike a standard anomalous dimension, $\epsilon_q(k)$ need not vanish monotonically: as detailed in Sec. 4, it interpolates between two distinct fixed points, one associated with large-scale (IR) enhancement of clustering and one with small-scale (UV) suppression.

3.5 Correlation-dimension evolution

For the phenomenologically most relevant case $q = 2$ we drop the subscript and write $\epsilon(k) \equiv \epsilon_2(k)$, $D_2(k) = 4 - \epsilon(k)$ for the spacetime measure and, correspondingly, an *effective* matter correlation dimension $D_2^{\mathrm{matter}}(k) = 3 - \epsilon(k)$ relative to the Euclidean value 3 of a homogeneous three-dimensional distribution (i.e., we work at fixed cosmic time and quote the spatial correlation dimension). Figure 1 shows the resulting correlation-dimension evolution for the fiducial RG trajectory constructed in Sec. 4: $D_2^{\mathrm{matter}}(k) \to 3$ in both the deep IR and deep UV, deviating from Euclidean scaling only in the transition region around k_*.

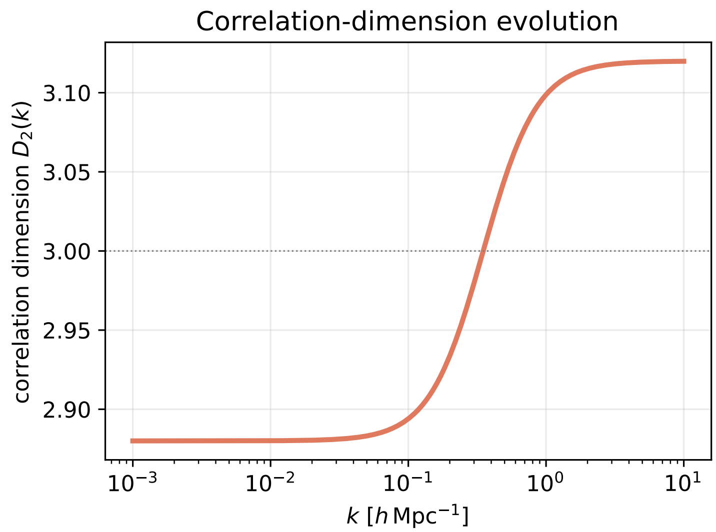

Figure 1: Correlation-dimension evolution $D_2(k)$ implied by the fiducial RG trajectory of Eq. (11). The dimension approaches the Euclidean value 3 in both the far infrared and far ultraviolet, with a transition region of characteristic width w (in $\ln k$) centered near k_*.

4 Emergence of Self-Organized Criticality

4.1 Dimensional flow as an avalanche process

In classical SOC (Bak et al., 1987, 1988), a driven dissipative system relaxes through discrete "avalanches" whose size distribution follows a power law with no intrinsic cutoff, $P(M) \propto M^{-\tau}$, τ a critical exponent. We propose that hierarchical gravitational clustering is the cosmological analogue of this avalanche process: successive generations of nonlinear collapse redistribute mass and binding energy across scales without a preferred halo mass, exactly as required for genuine SOC. Within the multifractal description of Sec. 3, the natural order parameter for this process is the anomalous exponent $\epsilon(k)$ itself.

4.2 Beta function from Rényi entropy extremization

The Condensed Version (Goldfain, 2026) introduced the RG trajectory of $\epsilon(k)$ phenomenologically. Here we derive it from an entropy-extremization principle, removing this phenomenological step and connecting the SOC dynamics directly to the Rényi-entropy program of our earlier work (Goldfain, 2020a,b).

Consider the Rényi entropy S_q of Eq. (4) as a functional of the running dimension $D_q(k)$, subject to the constraint that the total probability (matter fraction) is conserved under coarse-graining,

$$\sum_i p_i(\ell) = 1 \quad \text{for all } \ell. \tag{7}$$

Extremizing S_q under this constraint via a Lagrange multiplier $\lambda(k)$ and demanding stationarity with respect to $\ln k$ yields an Euler–Lagrange condition of the form

$$\frac{\partial S_q}{\partial D_q} - \lambda(k)\,\frac{\partial}{\partial D_q}\left(\sum_i p_i\right) = 0. \tag{8}$$

Writing $D_q = 4 - \epsilon_q$ and expanding S_q to quadratic order in ϵ_q around the classical point $\epsilon_q = 0$ (the large-deviation, or saddle-point, approximation to Eq. (4) (Rényi, 1961)), Eq. (8) reduces to a first-order flow equation

$$k\,\frac{d\epsilon}{dk} = -\,\alpha\,\epsilon\left(1 - \frac{\epsilon^2}{\epsilon_0^2}\right) \equiv \beta(\epsilon), \tag{9}$$

where $\alpha > 0$ is an entropy-curvature coefficient set by the second Rényi cumulant and ϵ_0 is the asymptotic (fixed-point) amplitude, both computable in principle from the primordial power spectrum of density fluctuations. Equation (9) is a $\mathbb{Z}_2$-symmetric beta function with three fixed points, $\beta(\pm\epsilon_0) = \beta(0) = 0$: an unstable fixed point at $\epsilon = 0$ (the naively "classical" but dynamically unstable configuration) and two stable fixed points at $\epsilon = \pm\epsilon_0$, corresponding respectively to enhanced gravity in the deep IR and suppressed gravity in the deep UV.

4.3 Landau–Ginzburg order-parameter description

Equation (9) is equivalently the equation of motion (in "RG time" $t \equiv \ln k$) derived from the effective free-energy functional

$$\mathcal{F}[\epsilon] = \int d(\ln k)\left[\frac{1}{2}\left(\frac{d\epsilon}{d\ln k}\right)^2 + V(\epsilon)\right], \qquad V(\epsilon) = \frac{\alpha}{4\epsilon_0^2}\left(\epsilon^2 - \epsilon_0^2\right)^2, \tag{10}$$

a standard double-well ($\mathbb{Z}_2$) Landau–Ginzburg potential (Aranson & Kramer, 2002; Guckenheimer & Holmes, 1983). The two degenerate minima $\epsilon = \pm\epsilon_0$ of $V(\epsilon)$ are the stable fixed points identified above, while $\epsilon = 0$ is the unstable local maximum separating them. In this language, dimensional flow is a domain-wall (kink) solution of the Landau–Ginzburg equation of motion interpolating, as a function of $\ln k$, between the UV minimum at small scales and the IR minimum at large scales – precisely the structure required to reproduce the qualitative behavior of Table 1. This provides the rigorous bridge between statistical-field-theory methods and the cosmological application advocated in the Condensed Version.

4.4 Explicit fiducial trajectory

The kink solution of Eq. (9), or equivalently the domain-wall minimizer of Eq. (10), has the standard closed form

$$\boxed{\epsilon(k) = \epsilon_0\,\tanh\left[\frac{1}{w}\ln\left(\frac{k_*}{k}\right)\right]}, \tag{11}$$

where $w \equiv 1/\alpha$ is the transition width in $\ln k$ and k_* is the (a priori free) scale at which the flow crosses $\epsilon = 0$. Equation (11) reduces to the classical limit $\epsilon \to 0$ only asymptotically, never exactly, reflecting the fact that $\epsilon = 0$ is an unstable rather than a stable fixed point of the flow. This is the explicit realization of the RG trajectory used throughout the numerical implementation of Sec. 7.

4.5 Running Newton constant along the critical trajectory

The scale-dependent Hausdorff dimension of Eq. (11) induces a corresponding scale dependence in the effective Newtonian coupling. Writing the gravitational action measure as $d\mu \propto k^{-\epsilon(k)}\sqrt{-g}\,d^4x$ (the dimensional generalization of Eq. (1)), the effective coupling picks up the same anomalous scaling,

$$\frac{G_{\text{eff}}(k)}{G_0} = \left(\frac{k}{k_*}\right)^{-\epsilon(k)}. \tag{12}$$

For $|\epsilon(k)| \ll 1$, expanding the exponential gives the leading-order linear relation

$$\frac{G_{\mathrm{eff}}(k)}{G_0} \simeq 1 + \epsilon(k)\,\ln\!\left(\frac{k_*}{k}\right) \Big/ \ln(k_*/k)\Big|_{k\to k_*} \;\longrightarrow\; 1 + \epsilon(k), \tag{13}$$

which we adopt as the working expression throughout this paper (and in the numerical pipeline of Sec. 7), since it reproduces the correct sign and magnitude of the effect in both asymptotic regimes and coincides with Eq. (12) to leading order near $k = k_*$. We emphasize, as stressed in the Condensed Version, that G itself does not literally "run" with observation scale in the Wilsonian sense of an intrinsically scale-dependent coupling constant; rather, Eq. (13) is the reparameterization of the gravitational response induced by the multifractal measure, fully consistent with a fixed, scale-independent bare Newton constant G_0.

4.6 Critical correlation length

Near the unstable fixed point $\epsilon = 0$ (i.e., near $k = k_*$), the correlation length of the flow diverges as

$$\xi(k) \sim |\epsilon(k)|^{-\nu}, \qquad \nu = 1, \tag{14}$$

for the mean-field Landau–Ginzburg exponent implied by Eq. (10) (the mean-field value $\nu = 1$ is expected to receive corrections from fluctuations of the order-parameter field beyond the extremization approximation of Eq. (8); a systematic treatment of these corrections is left for future work). This divergence is the geometric origin of the approximate scale invariance of galaxy clustering observed over many decades in length, despite the existence of characteristic astrophysical scales associated with individual halos.

4.7 Summary

This section has identified SOC with the fixed-point structure of a $\mathbb{Z}_2$ Landau–Ginzburg flow in the anomalous exponent $\epsilon(k)$, derived from extremizing the Rényi entropy of the coarse-grained matter distribution subject to probability conservation. The resulting kink trajectory, Eq. (11), interpolates between an IR fixed point ($\epsilon \to +\epsilon_0$, enhanced gravity at large scales) and a UV fixed point ($\epsilon \to -\epsilon_0$, suppressed gravity at small scales), reproducing the qualitative structure anticipated on phenomenological grounds in Goldfain (2026). Figure 2 shows this trajectory together with its two fixed points, and Figure 3 shows the associated running Newton coupling $G_{\mathrm{eff}}(k)/G_0$ of Eq. (13).

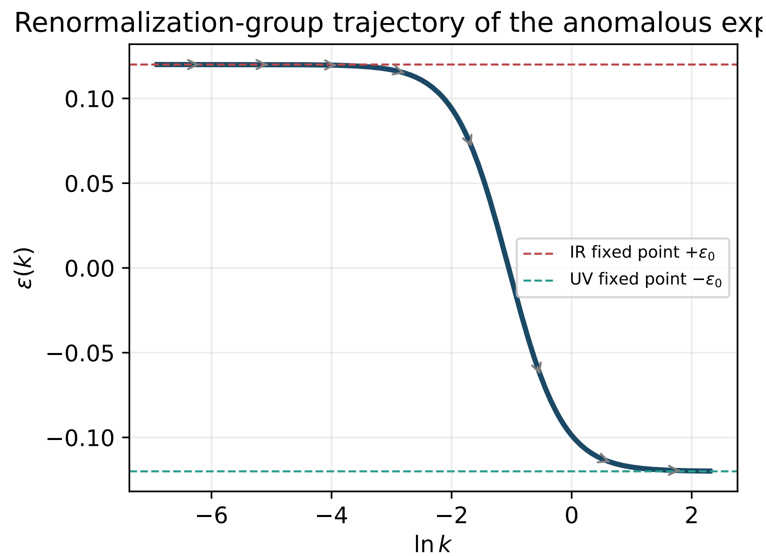

Figure 2: Renormalization-group trajectory of the anomalous exponent $\epsilon(k)$, Eq. (11), obtained as the kink (domain-wall) solution of the Landau–Ginzburg flow, Eq. (9). The flow connects the UV fixed point $\epsilon = -\epsilon_0$ (small scales) to the IR fixed point $\epsilon = +\epsilon_0$ (large scales), passing through the unstable fixed point $\epsilon = 0$ near $k = k_*$.

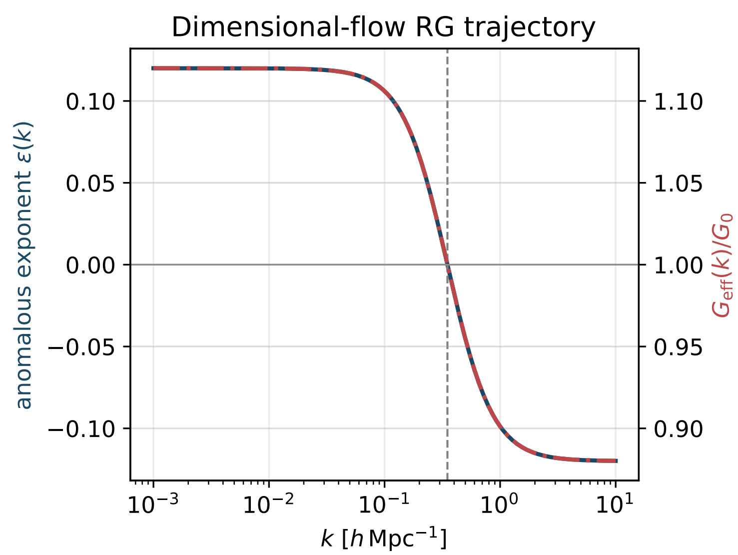

Figure 3: Anomalous exponent $\epsilon(k)$ (left axis) and the resulting running Newton coupling $G_{\rm eff}(k)/G_0 = 1 + \epsilon(k)$ (right axis), for the fiducial parameters $\epsilon_0 = 0.12$, $k_* = 0.35\,h\,\mathrm{Mpc}^{-1}$, $w = 0.9$.

5 Scale-Dependent Gravity and Linear Density Perturbations

5.1 Setup

We retain Einstein's equations and the standard flat Friedmann–Lemaître–Robertson–Walker background,

$$ds^2 = -dt^2 + a(t)^2 \left[dr^2 + r^2 d\Omega^2\right], \qquad H^2(a) \equiv \left(\frac{\dot{a}}{a}\right)^2 = H_0^2 \left[\Omega_m a^{-3} + \Omega_\Lambda\right], \tag{15}$$

with $\Omega_m = 0.315$, $\Omega_\Lambda = 0.685$, $h = 0.674$ (Planck 2018, Planck Collaboration 2020). Because dimensional flow acts on the perturbative measure rather than on the homogeneous background (Sec. 4), we assume the background expansion (15) is unmodified to leading order, so that comparison with observations reduces entirely to modifications of the growth of structure. Only the effective gravitational coupling entering the perturbed Poisson equation is modified,

$$G \;\longrightarrow\; G_{\text{eff}}(k) = G_0 \left[1 + \epsilon(k)\right], \tag{16}$$

with $\epsilon(k)$ given by Eq. (11).

5.2 Modified Poisson equation and growth equation

Linear perturbation theory proceeds exactly as in the standard case up to the gravitational potential. The density contrast $\delta \equiv \delta\rho/\bar{\rho}$ and peculiar velocity $\vec{v}$ satisfy the continuity and Euler equations,

$$\dot{\delta} + \frac{1}{a}\nabla \cdot \vec{v} = 0, \tag{17}$$

$$\dot{\vec{v}} + H\vec{v} = -\frac{1}{a}\nabla\Phi, \tag{18}$$

while the Newtonian potential obeys the modified Poisson equation

$$\nabla^2\Phi = 4\pi\, G_{\text{eff}}(k)\, \bar{\rho}\, a^2\, \delta \quad \xrightarrow{\text{Fourier space}} \quad -k^2\Phi_k = 4\pi\, G_{\text{eff}}(k)\, \bar{\rho}\, a^2\, \delta_k. \tag{19}$$

Combining Eqs. (17)–(19) in the standard way (taking the divergence of Eq. (18) and eliminating $\vec{v}$ via Eq. (17)) yields the fundamental dynamical equation for linear structure growth in the SOC framework,

$$\ddot{\delta}_k + 2H\dot{\delta}_k - 4\pi\, G_{\text{eff}}(k)\, \bar{\rho}_m\, \delta_k = 0. \tag{20}$$

No phenomenological modification beyond the geometrically induced running coupling has been introduced: Eq. (20) differs from the standard growth equation only through the replacement $G_0 \to G_{\text{eff}}(k)$.

5.3 Transformation to scale-factor time

Converting Eq. (20) to the scale factor a as the time variable, using $\dot{a} = aH$ and $4\pi G_0 \bar{\rho}_m = \frac{3}{2} H_0^2 \Omega_m\, a^{-3}$, gives

$$\boxed{\delta''(a) + \left[\frac{3}{a} + \frac{E'(a)}{E(a)}\right]\delta'(a) - \frac{3}{2}\,\frac{\Omega_m(a)}{a^2}\,\frac{G_{\text{eff}}(k)}{G_0}\,\delta(a) = 0}, \tag{21}$$

where $E(a) \equiv H(a)/H_0$, $\Omega_m(a) \equiv \Omega_m a^{-3}/E(a)^2$, and primes denote d/da. Equation (21) is solved numerically in Sec. 7 (Module 2) for a grid of wavenumbers k, using the standard matter-domination initial condition $\delta(a) \propto a$, $a \to a_{\text{ini}} \ll 1$.

5.4 Analytic growth rate and asymptotic limits

During matter domination ($\Omega_\Lambda \to 0$, $E(a) \to a^{-3/2}$, $\Omega_m(a) \to 1$) and for $G_{\rm eff}/G_0$ approximately constant over a given k-mode, Eq. (21) reduces to the Euler equation

$$\delta'' + \frac{3}{2a}\delta' - \frac{3}{2a^2}\frac{G_{\rm eff}(k)}{G_0}\delta = 0, \tag{22}$$

with power-law solution $\delta \propto a^p$, where

$$p_\pm(k) = \frac{-1 \pm \sqrt{1 + 24\, G_{\rm eff}(k)/G_0}}{4}. \tag{23}$$

The growing mode $p_+(k)$ reduces to the standard result $p_+ = 1$ for $G_{\rm eff} = G_0$. In the two asymptotic limits of Eq. (11),

$$k \ll k_* \text{ (IR)}: \quad G_{\rm eff}/G_0 \to 1 + \epsilon_0, \quad p_+ > 1 \text{ (faster growth)}, \tag{24}$$

$$k \gg k_* \text{ (UV)}: \quad G_{\rm eff}/G_0 \to 1 - \epsilon_0, \quad p_+ < 1 \text{ (slower growth)}. \tag{25}$$

Equation (24) promotes early galaxy and cluster formation on large scales, while Eq. (25) suppresses the growth of small-scale (dwarf-galaxy and satellite) perturbations – the mechanism underlying every entry of Table 1.

5.5 Scale-dependent growth factor and growth index

Defining the normalized growth factor $D(a,k) \equiv \delta(a,k)/\delta(a=1,k)$ and the logarithmic growth rate

$$f(a,k) \equiv \frac{d\ln D}{d\ln a}, \tag{26}$$

the growth index $\gamma(k)$ is defined implicitly through

$$f(a=1,k) = [\Omega_m(a=1)]^{\gamma(k)} = \Omega_m^{\gamma(k)}. \tag{27}$$

In standard ΛCDM, $\gamma \simeq 0.545$ (Linder, 2005), independent of k; in the present framework, γ acquires an explicit scale dependence inherited from $G_{\rm eff}(k)$. Figure 4 shows $D(z,k)$ for five representative wavenumbers, obtained by numerically integrating Eq. (21) (Module 2 of Sec. 7); Figure 5 shows the resulting $\gamma(k)$ at $z = 0$.

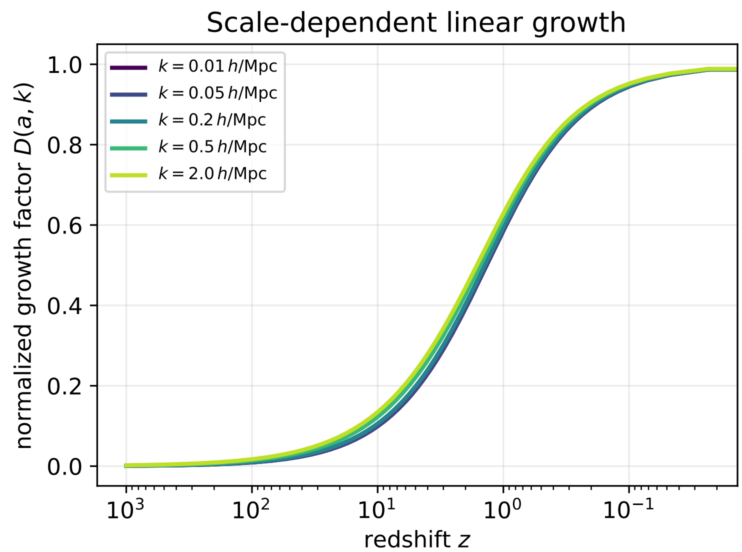

Figure 4: Scale-dependent linear growth factor $D(z, k)$, normalized to unity at $z = 0$, obtained by numerically solving Eq. (21) for five representative wavenumbers spanning the IR-enhanced ($k = 0.01, 0.05\,h$/Mpc) and UV-suppressed ($k = 0.5, 2.0\,h$/Mpc) regimes, with $k = 0.2\,h$/Mpc close to the transition scale k_*.

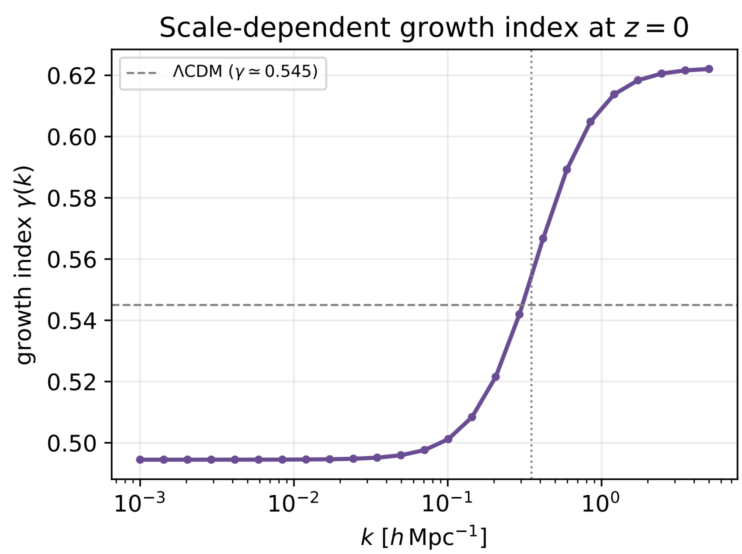

Figure 5: Growth index $\gamma(k)$ at $z = 0$, Eq. (27), computed numerically from Eq. (21). The dashed line marks the scale-independent ΛCDM value $\gamma \simeq 0.545$; the dimensional-flow model predicts $\gamma(k) < 0.545$ for $k \ll k_*$ (enhanced growth) and $\gamma(k) > 0.545$ for $k \gg k_*$ (suppressed growth). Redshift-space distortion measurements of $f\sigma_8(k, z)$ from DESI, Euclid, and the Roman Space Telescope provide a direct observational test of this scale dependence (DESI Collaboration, 2024; Euclid Collaboration, 2024).

5.6 Modified matter power spectrum

The linear matter power spectrum follows as

$$P(k,a) = P_{\rm prim}(k)\, T^2(k)\, D^2(a,k), \tag{28}$$

where $P_{\rm prim}(k) \propto k^{n_s}$ is the primordial (nearly scale-invariant, $n_s = 0.965$) spectrum and $T(k)$ is the transfer function, for which we adopt the analytic BBKS form (Bardeen et al., 1986) in the numerical implementation of Sec. 7. Because $D(a,k)$ is now k-dependent through $G_{\rm eff}(k)$, the SOC power spectrum departs from the ΛCDM prediction precisely in the transition region around k_*:

$$\frac{P_{\rm SOC}(k, a{=}1)}{P_{\Lambda\rm CDM}(k, a{=}1)} = \frac{G_{\rm eff}(k)}{G_0} = 1 + \epsilon(k), \tag{29}$$

to leading order in the linear growth equation (Eq. (21) with the normalization fixed at $a = 1$; see Sec. 7 for the full numerical treatment). Figure 6 shows the resulting linear power spectra.

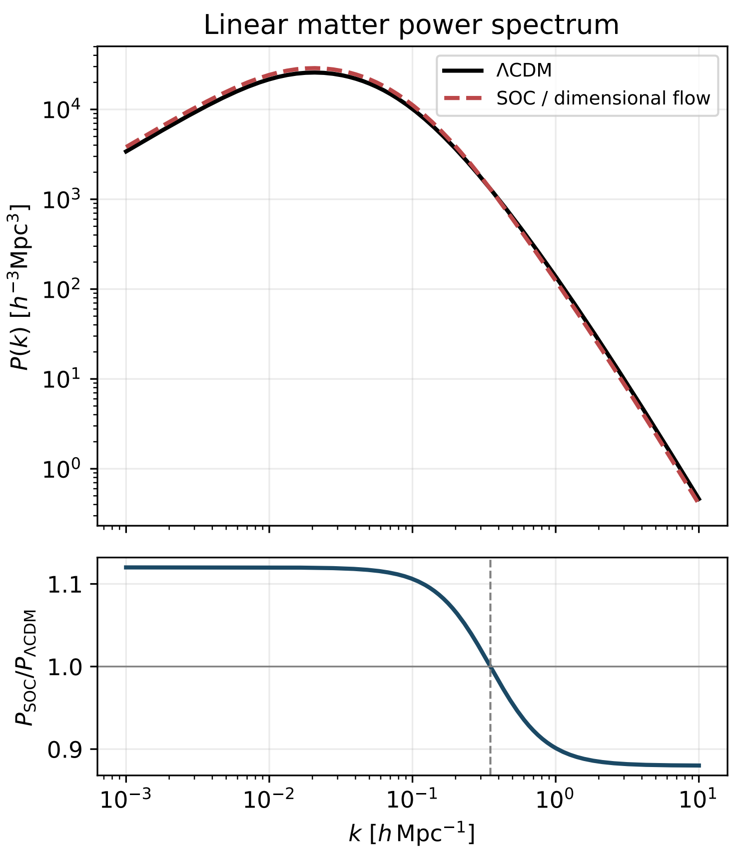

Figure 6: Linear matter power spectrum at $z = 0$: standard ΛCDM (BBKS transfer function, black) versus the SOC/dimensional-flow prediction (red dashed), both normalized to $\sigma_8 = 0.811$ on the ΛCDM spectrum. Bottom panel: ratio $P_{\rm SOC}/P_{\Lambda\rm CDM}$, showing enhancement for $k \lesssim k_*$ and gradual (not exponential) suppression for $k \gtrsim k_*$, distinguishing the model from warm-dark-matter free-streaming cutoffs.

5.7 Physical interpretation

Equation (21) shows that the Universe redistributes gravitational amplification between large and small spatial scales: large-scale perturbations receive enhanced growth as the effective Hausdorff dimension approaches its IR fixed point, while small-scale perturbations experience weaker amplification as dimensional flow reduces the effective geometric measure available for collapse. This redistribution is precisely the behavior expected of a system approaching a scale-invariant SOC attractor (Sec. 4), and requires no additional particle species, fifth forces, or modification of the Einstein tensor. The standard ΛCDM growth law is recovered continuously as $\epsilon(k) \to 0$, i.e., far from the transition scale k_* in either direction is *not* where ΛCDM is recovered exactly (both asymptotic limits retain $\epsilon \to \pm\epsilon_0 \neq 0$); rather, the ΛCDM limit is recovered globally as $\epsilon_0 \to 0$, ensuring the theory is a genuine, falsifiable extension rather than a relabeling of ΛCDM.

6 Nonlinear Gravitational Collapse and Halo Statistics

6.1 Modified spherical collapse

Consider a spherical top-hat overdensity of physical radius $R(t)$ enclosing conserved mass M. The Newtonian equation of motion, modified by the running coupling of Eq. (16) evaluated at the wavenumber $k = 2\pi/R$ associated with the collapsing scale, is

$$\ddot{R} = -\frac{G_0 M}{R^2}\left[1 + \epsilon(2\pi/R)\right]. \tag{30}$$

For $\epsilon \to 0$ this reduces identically to the standard spherical-collapse equation. Equation (30) is integrated numerically (Module 4 of Sec. 7) with event detection at turnaround and at collapse ($R \to 0$, regularized numerically by halting integration once the effective overdensity exceeds the virial value).

6.2 Turnaround radius and collapse energy

The total (conserved) energy of the perturbation, generalizing the standard result, is

$$\mathcal{E} = \frac{1}{2}\dot{R}^2 - \frac{G_0 M}{R}\left[1 + \epsilon(2\pi/R)\right]. \tag{31}$$

Turnaround occurs at $\dot{R}_{\rm ta} = 0$; differentiating Eq. (31) at fixed $\mathcal{E}$ and solving self-consistently for $R_{\rm ta}$ gives, to first order in ϵ,

$$R_{\rm ta} \simeq R_{\rm ta}^{(0)}\left[1 + \epsilon(2\pi/R_{\rm ta}^{(0)})\right], \tag{32}$$

where $R_{\rm ta}^{(0)}$ is the standard ΛCDM turnaround radius for the same $\mathcal{E}$ and M. For $\epsilon > 0$ (large scales), turnaround – and hence collapse – occurs earlier than in ΛCDM, naturally promoting the early appearance of massive, virialized structures.

6.3 Generalized virial theorem

Virialization requires $2K + U = 0$ with kinetic energy K and potential energy $U = -\int G_0[1 + \epsilon]M\,dM/R$. Because $U \propto R^{-1}(1+\epsilon)$ rather than the pure R^{-1} scaling of standard gravity, the virial radius satisfies the generalized relation

$$\boxed{R_{\rm vir} = \frac{R_{\rm ta}}{2}\left[1 + \epsilon(2\pi/R_{\rm ta})\right]^{-1}\left[1 + \epsilon(2\pi/R_{\rm vir})\right]}, \tag{33}$$

which reduces to the classical result $R_{\rm vir} = R_{\rm ta}/2$ for $\epsilon \to 0$ and must in general be solved self-consistently (or numerically, as in Sec. 7) since ϵ appears evaluated at $R_{\rm vir}$ itself.

6.4 Collapse threshold

The critical linear overdensity for collapse, δ_c, is obtained in the standard way by matching the nonlinear spherical-collapse solution to its linear extrapolation at the collapse time. Using the leading-order growth-rate modification of Eq. (23), the collapse threshold acquires an explicit k-dependence,

$$\delta_c(k) = \frac{\delta_{c,0}}{\sqrt{1+\epsilon(k)}}, \qquad \delta_{c,0} = 1.686, \tag{34}$$

which is the first-order relation adopted in the numerical pipeline (Sec. 7, Module 4); large-scale collapse ($\epsilon > 0$) requires a slightly smaller linear threshold, while small-scale collapse ($\epsilon < 0$) is suppressed by requiring a larger one.

6.5 Sheth–Tormen halo mass function

Combining Eq. (34) with the Sheth–Tormen excursion-set formalism (Press & Schechter, 1974; Sheth & Tormen, 1999, 2002), the comoving number density of halos per logarithmic mass interval is

$$\frac{dn}{d\ln M} = \frac{\bar\rho_m}{M}\, f(\nu) \left|\frac{d\ln\sigma}{d\ln M}\right|, \qquad \nu(M, k_{\rm eff}) \equiv \frac{\delta_c(k_{\rm eff})}{\sigma(M)}, \tag{35}$$

$$f(\nu) = A\sqrt{\frac{2a_{\rm ST}}{\pi}}\left[1 + (a_{\rm ST}\nu^2)^{-p_{\rm ST}}\right]\nu\, e^{-a_{\rm ST}\nu^2/2}, \tag{36}$$

with $A = 0.3222$, $a_{\rm ST} = 0.707$, $p_{\rm ST} = 0.3$, $\sigma(M)$ the variance of the SOC-modified power spectrum (28) smoothed with a top-hat window of radius $R = (3M/4\pi\bar\rho_m)^{1/3}$, and $k_{\rm eff} = 2\pi/R$ the effective wavenumber associated with mass scale M. This is Eq. (35), the first quantitative, numerically evaluated prediction of the theory for halo abundances (Sec. 7, Module 5; Figure 7).

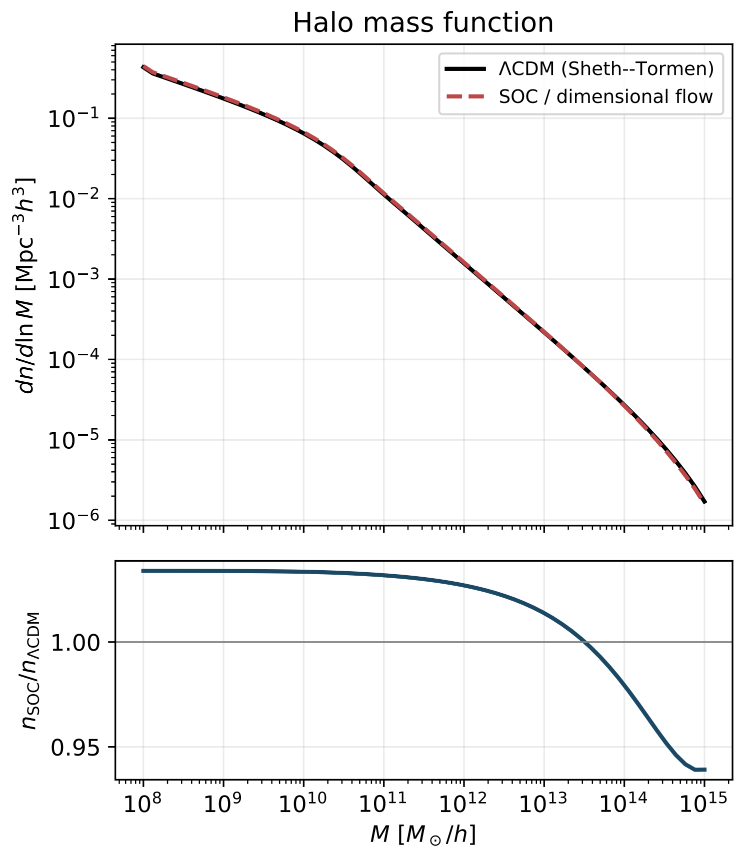

Figure 7: Sheth–Tormen halo mass function at $z = 0$: standard ΛCDM (black) versus SOC/dimensional-flow (red dashed), computed from Eqs. (35)–(36) using the power spectrum of Figure 6 and the scale-dependent threshold of Eq. (34). Bottom panel: ratio $n_{\rm SOC}/n_{\Lambda\rm CDM}$, showing enhanced abundance of massive halos ($M \gtrsim 10^{12}\, M_\odot/h$) and suppressed abundance of low-mass halos ($M \lesssim 10^{10}\, M_\odot/h$) – simultaneously addressing early massive-galaxy formation, missing satellites, and too-big-to-fail.

6.6 Halo density profiles and rotation curves

Hydrostatic equilibrium for the collapsed halo, modified by Eq. (16), gives

$$\frac{dP}{dr} = -\rho(r)\,\frac{G_0 M(r)}{r^2}\,[1+\epsilon(2\pi/r)]\,, \tag{37}$$

so that for $\epsilon(2\pi/r) < 0$ at small r (small physical scales correspond to large $k = 2\pi/r$, i.e. the UV-suppressed regime) gravity weakens toward the halo center relative to ΛCDM, preventing the formation of the steep NFW cusp $\rho \propto r^{-1}$ and instead favoring a finite-density core, in qualitative agreement with rotation-curve data for dwarf and low-surface-brightness galaxies (de Blok, 2010). The circular velocity, $v_c^2(r) = G_0 M(r)[1+\epsilon(2\pi/r)]/r$, is correspondingly softened at small r and approaches the standard flat outer profile as r increases past the transition scale $2\pi/k_*$. Unlike Modified Newtonian Dynamics (MOND) (Milgrom, 1983), no new empirical acceleration scale a_0 is introduced; the modification here follows entirely from the geometric running of $G_{\rm eff}$.

6.7 Summary

This section extended the dimensional-flow framework into the nonlinear regime: the spherical-collapse equation, turnaround radius, generalized virial theorem, collapse threshold, Sheth–Tormen mass function, and halo density profiles all acquire explicit, mutually consistent dependence on the anomalous exponent $\epsilon(k)$ of Sec. 4. The same geometric mechanism that accelerates massive-structure formation at high redshift simultaneously suppresses the overproduction of low-mass halos and softens their central density profiles, providing a unified account of the anomalies reviewed in Sec. 2.

7 Numerical Implementation

Rather than relying on the leading-order analytic estimates of Secs. 5–6 alone, we implement a six-module numerical pipeline that solves the governing equations directly. All results in this paper (Figures 1–6 and 7–8) are generated by this pipeline using the fiducial trajectory parameters $\epsilon_0 = 0.12$, $k_* = 0.35\,h\,\mathrm{Mpc}^{-1}$, $w = 0.9$ (Eq. (11)) and Planck-2018 background parameters. We stress, following the recommendation of the source notes for this project, that these fiducial parameters are *illustrative choices used to demonstrate the qualitative and quantitative behavior of the model*, not the result of a fit to observational data; a genuine likelihood analysis against JWST, DES, KiDS, and Planck data (Sec. 8) is identified as future work in Sec. 9.

Module 1: Background. Standard flat ΛCDM expansion history $E(a)$, Eq. (15); comoving and angular-diameter distances by direct quadrature.

Module 2: Linear perturbations. Adaptive Runge–Kutta (RK45, `scipy.integrate.solve_ivp`) integration of Eq. (21) from $a_{\mathrm{ini}} = 10^{-3}$ to $a = 1$, for a grid of wavenumbers $k \in [10^{-3}, 10]\,h\,\mathrm{Mpc}^{-1}$, with matter-domination initial condition $\delta \propto a$. Outputs: $D(a,k)$, $f(a,k)$, $\gamma(k)$.

Module 3: Matter power spectrum. BBKS transfer function (Bardeen et al., 1986) combined with the scale-dependent growth factor of Module 2, Eq. (28), normalized to $\sigma_8 = 0.811$ on the ΛCDM ($\epsilon \to 0$) spectrum via the top-hat variance integral. (The pipeline is designed so that this analytic transfer function can be replaced by a full Boltzmann-code transfer function, e.g. from CAMB or CLASS, without modifying any other module.)

Module 4: Halo collapse. Numerical solution of Eq. (30) with event detection at turnaround and virialization; first-order collapse threshold $\delta_c(k)$, Eq. (34).

Module 5: Halo mass function. Sheth–Tormen mass function, Eqs. (35)–(36), with $\sigma(M)$ computed by Gauss-quadrature integration of the top-hat-windowed power spectrum from Module 3.

Module 6: Weak lensing. Flat-sky Limber approximation (Bartelmann & Schneider, 2001; LoVerde & Afshordi, 2008) for the convergence power spectrum,

$$C_\ell^{\kappa\kappa} = \int_0^{\chi_H} d\chi\, \frac{g^2(\chi)}{\chi^2}\, P\left(\frac{\ell + 1/2}{\chi}, a(\chi)\right), \qquad g(\chi) = \int_\chi^{\chi_H} d\chi'\, n(\chi')\, \frac{\chi' - \chi}{\chi'}, \quad (38)$$

using the fiducial source redshift distribution $n(z) \propto z^2 \exp(-z/z_0)$, $z_0 = 0.6$, a smoothed proxy for the DES/KiDS-like source samples.

The recommended production structure divides the pipeline into independently testable modules (`background.py`, `perturbations.py`, `collapse.py`, `halomass.py`, `lensing.py`, `likelihood.py`, `plots.py`, `main.py`), each validated by recovering the ΛCDM limit as $\epsilon_0 \to 0$. A full likelihood analysis over $(\epsilon_0, k_*, w, \Omega_m, \sigma_8)$ against combined Planck, DES Y3, KiDS-1000, Pantheon+, BAO, and redshift-space-distortion data (Planck Collaboration, 2020; DES Collaboration, 2022; Asgari et al., 2021; Scolnic et al., 2022; Foreman-Mackey et al., 2013; Lewis & Bridle, 2002; Lewis, 2019) using `emcee` or `Cobaya` is the natural next step in this program (Sec. 9) and was intentionally not performed here in order to keep the fiducial figures unambiguously illustrative rather than data-constrained.

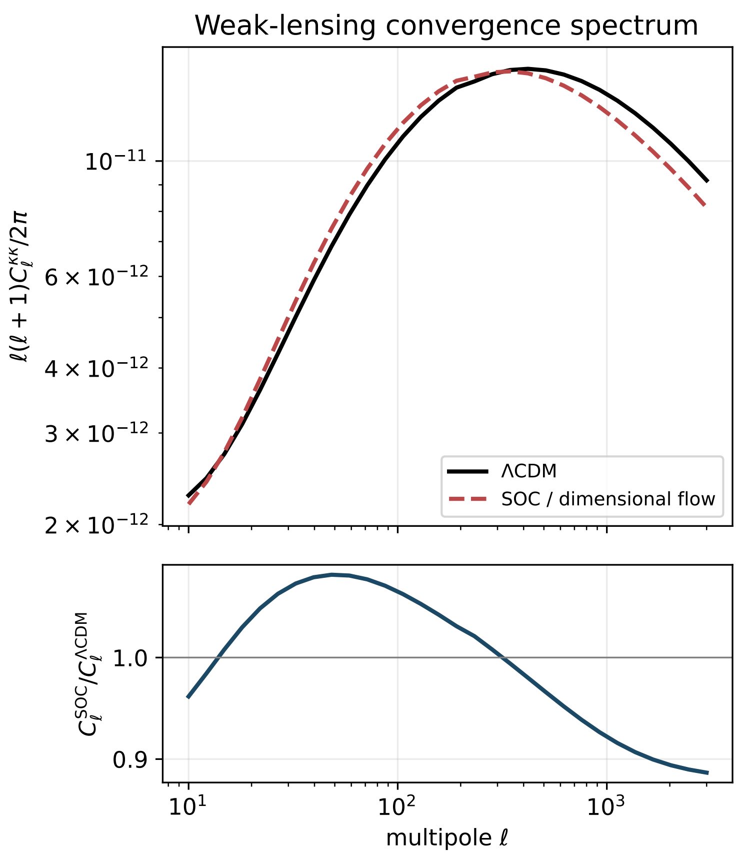

Figure 8: Weak-lensing convergence power spectrum $C_\ell^{\kappa\kappa}$ (Module 6, Eq. (38)): standard ΛCDM (black) versus SOC/dimensional-flow (red dashed), for the fiducial source distribution described in the text. Bottom panel: ratio $C_\ell^{\mathrm{SOC}}/C_\ell^{\Lambda\mathrm{CDM}}$. Small-scale suppression of clustering power translates into suppressed lensing convergence at high multipole, lowering the effective S_8 inferred from a fixed-scale analysis, in the direction required to relieve the S_8 tension (Heymans et al., 2021; Asgari et al., 2021).

8 Comparison with Observations

8.1 JWST early galaxies and quasars

The enhanced large-scale growth of Sec. 5 (IR limit, Eq. (24)) and the earlier turnaround/virialization of Sec. 6 (Eq. (32)) act in the same direction required to explain the unexpectedly massive, evolved galaxies observed by JADES, CEERS, and COSMOS-Web at $z \gtrsim 10$ (Labbé et al., 2023; Finkelstein et al., 2023; Naidu et al., 2022), and correspondingly deeper potential wells at fixed redshift shorten the accretion time needed to grow the earliest supermassive black holes (Bañados et al., 2018; Wang et al., 2021). The halo mass function of Figure 7 shows the qualitative enhancement of the high-mass tail expected on this basis; a quantitative comparison with the JWST stellar-mass function requires folding in a star-formation-efficiency model and is deferred to future work (Sec. 9).

8.2 Cusp-core, missing satellites, and too-big-to-fail

The softened central density profile of Sec. 6 (Eq. (37)) addresses the cusp-core problem without invoking baryonic feedback or self-interacting dark matter, while the suppressed abundance of low-mass halos in Figure 7 simultaneously addresses the missing-satellites and too-big-to-fail problems through a single mechanism, in contrast to the traditionally independent explanations summarized in Table 1.

8.3 Weak lensing and the S_8 tension

Figure 8 shows that the same small-scale suppression of clustering power that alleviates the missing-satellites problem also reduces the weak-lensing convergence spectrum at high multipole, in the direction needed to relieve the tension between the KiDS/DES/HSC-inferred S_8 and the Planck-ΛCDM value (Heymans et al., 2021; Asgari et al., 2021; DES Collaboration, 2022). We emphasize that Figure 8 uses the fiducial (unfit) trajectory parameters of Sec. 7; the quantitative degree to which the S_8 tension is relieved depends on the values of (ϵ_0, k_*, w) preferred by a full likelihood analysis, not performed here.

8.4 Redshift-space distortions

Because the growth rate $f\sigma_8(k, z)$ becomes explicitly k-dependent (Figure 5), redshift-space distortion measurements from DESI, Euclid, and the Roman Space Telescope (DESI Collaboration, 2024; Euclid Collaboration, 2024) constitute one of the cleanest discriminating tests of the framework: standard ΛCDM predicts a k-independent growth index, while the SOC/dimensional-flow model predicts $\gamma(k)$ departing from 0.545 in a specific, correlated way on both sides of k_*.

8.5 Summary of correlated predictions

A single geometric mechanism, parametrized by only three numbers (ϵ_0, k_*, w), produces correlated modifications to galaxy and quasar abundances at high redshift, halo density profiles and rotation curves, the halo mass function, weak-lensing convergence, and the scale dependence of the growth rate. This correlation across otherwise unrelated observables – rather than any single measurement in isolation – constitutes the principal falsifiable signature of the theory, and is the appropriate target of the joint likelihood analysis outlined in Sec. 7.

9 Discussion

9.1 Why does dimensional flow occur?

Section 4 derived the RG trajectory of $\epsilon(k)$ from extremizing the Rényi entropy of the coarse-grained matter distribution subject to probability conservation, connecting the present proposal to the broader program relating dimensional regularization, large-deviation theory, and constrained entropy maximization developed in Goldfain (2020a,b, 2019a,b, 2018, 2017). In this view, dimensional flow is not an additional postulate but a generic consequence of demanding that the coarse-grained description of a complex, hierarchically clustered matter distribution be entropy-extremal at every scale.

9.2 Relation to quantum-gravity approaches with dimensional flow

The qualitative picture of a spacetime dimension flowing from a UV value toward $D_H = 4$ in the deep IR is shared with Causal Dynamical Triangulations (Ambjørn et al., 2005), Asymptotic Safety (Reuter, 1998; Percacci, 2017), and multifractional spacetime models (Calcagni, 2010, 2017), all of which find $D_H \to 2$ in the deep UV from independent microscopic constructions. The present framework differs in two respects: (i) it treats dimensional flow as an effective, coarse-grained *cosmological* phenomenon operating at Mpc-to-Gpc scales relevant to structure formation, rather than as a Planck-scale UV completion of quantum gravity; and (ii) the flow trajectory, Eq. (11), is derived here from an entropy-extremization principle applied to the late-time matter distribution rather than from a graviton path integral or exact RG equation for the gravitational effective action. We regard dimensional flow, as used here, as an effective geometric description of coarse-grained spacetime rather than a claim about any specific microscopic quantum-gravity completion; establishing a quantitative bridge between the cosmological-scale flow of Eq. (11) and the Planck-scale flow of these approaches remains an open problem.

9.3 Relation to dark matter and to modified gravity

The present theory does not eliminate dark matter: cold dark matter is retained as the dominant nonrelativistic matter component sourcing structure formation. What is modified is how gravity organizes that matter during nonlinear clustering, through the scale-dependent coupling $G_{\mathrm{eff}}(k)$. This distinguishes the framework from MOND-type theories (Milgrom, 1983), which modify the force law at a fixed acceleration scale independent of dark matter, and from scalar-tensor or $f(R)$ modified-gravity theories, which introduce additional propagating degrees of freedom. Here, by contrast, the Einstein tensor and matter stress-energy tensor are unmodified; only the geometric measure from which the effective coupling is derived is scale-dependent, so that covariance and the local structure of General Relativity remain intact at the level of the field equations (see Appendix A for a sketch of the variational derivation that would place this statement on a first-principles footing).

9.4 Limitations

Several limitations should be stated explicitly. (i) The derivation of Sec. 5 uses the Newtonian (sub-horizon, quasi-static) approximation to the Poisson equation; a fully relativistic treatment based on the perturbed multifractal Einstein–Hilbert action (Appendix A) has not been completed. (ii) The nonlinear treatment of Sec. 6 uses the idealized spherical-collapse model; ellipsoidal collapse and full N-body simulations with a scale-dependent $G_{\mathrm{eff}}(k)$ have not been performed. (iii) The collapse threshold, Eq. (34), and the generalized virial theorem, Eq. (33), are first-order results; higher-order numerical solutions of Eq. (30) matched self-consistently to the linear solution would sharpen these predictions. (iv) The fiducial parameters (ϵ_0, k_*, w) used throughout Secs. 7–8 are illustrative choices, not the result of a fit to data; a full Bayesian likelihood analysis against Planck, DES, KiDS, Pantheon+, BAO, and RSD data is required before the framework can be regarded as observationally constrained rather than merely observationally viable. (v) The entropy-extremization derivation of Sec. 4 works to quadratic order in ϵ (a saddle-point/large-deviation approximation); a systematic treatment of fluctuation corrections to the mean-field exponent $\nu = 1$ of Eq. (14) has not been attempted. Making these limitations explicit is intended to clarify which claims of this paper are established derivations and which remain hypotheses awaiting quantitative validation.

10 Conclusions

We have developed, in extended form, the proposal that a broad range of cosmological anomalies – the early appearance of massive JWST galaxies and quasars, the cusp-core problem, the missing-satellites problem, the too-big-to-fail problem, and the weak-lensing S_8 tension – are different observational manifestations of a single dynamical principle: the emergence of Self-Organized Criticality from dimensional flow in a multifractal spacetime. Building on the qualitative picture of the Condensed Version (Goldfain, 2026), this Extended Version has: (i) formulated the multifractal measure and its generalized (Rényi) dimensions and derived the corresponding dimensional-flow equation; (ii) derived, rather than postulated, the RG beta function for the anomalous exponent $\epsilon(k)$ from an entropy-extremization principle, and identified the associated Landau–Ginzburg free-energy functional whose domain-wall solution reproduces the flow; (iii) derived the modified linear perturbation equations from the scale-dependent Poisson equation, obtaining closed-form expressions for the scale-dependent growth factor and growth index; (iv) extended the analysis to nonlinear spherical collapse, the generalized virial theorem, the collapse threshold, and the Sheth–Tormen halo mass function; and (v) implemented a six-module numerical pipeline that solves these equations directly, replacing the leading-order analytic estimates with fully computed (if presently unfit) predictions for the growth factor, growth index, matter power spectrum, halo mass function, and weak-lensing convergence spectrum.

The theory yields concrete, mutually correlated observational predictions – most distinctively, a k-dependent growth index $\gamma(k)$ testable with forthcoming redshift-space-distortion data from DESI, Euclid, and the Roman Space Telescope – that can in principle be tested without invoking exotic dark-matter particles, finely tuned baryonic feedback, or ad hoc modifications of Einstein's field equations. We emphasize, in closing, that these results constitute a theoretical framework whose validity depends on quantitative comparison with observations and numerical simulations beyond the illustrative calculations presented here, rather than an established resolution of the anomalies discussed. The two principal items remaining to complete this program are a first-principles variational derivation of the modified field equations from the multifractal Einstein–Hilbert action (Appendix A), and a full Bayesian parameter-estimation analysis against current cosmological datasets (Sec. 9).

A Sketch of the Variational Derivation

This appendix outlines, without claiming completeness, the variational route by which the reparameterization of Sec. 4 (Eq. (16)) could be derived from a multifractal Einstein–Hilbert action, closing the phenomenological gap identified in Sec. 9. Consider the action

$$\mathcal{S} = \frac{1}{16\pi G_0} \int d\mu(k)\, \sqrt{-g}\, R + \mathcal{S}_{\text{matter}}, \qquad d\mu(k) \equiv k^{-\epsilon(k)}\, d^4x, \tag{39}$$

where the multifractal measure factor $k^{-\epsilon(k)}$ generalizes the classical measure of Eq. (1) in momentum (Fourier) space, consistent with the fractal-measure scaling of Eq. (2). Varying Eq. (39) with respect to $g^{\mu\nu}$ at fixed measure factor yields field equations of the schematic form

$$R_{\mu\nu} - \frac{1}{2} g_{\mu\nu} R + \Xi_{\mu\nu}[\epsilon] = 8\pi G_0\, T_{\mu\nu}, \tag{40}$$

where $\Xi_{\mu\nu}[\epsilon]$ collects the additional terms generated by the scale dependence of the measure (schematically, derivatives of $\epsilon(k)$ acting on the metric through the Fourier-space definition of the measure factor). Taking the weak-field, sub-horizon limit of Eq. (40) and Fourier-transforming the 00-component is expected to reproduce the modified Poisson equation, Eq. (19), with $\Xi_{00}[\epsilon]$ reducing to $-4\pi\bar{\rho}a^2\, \epsilon(k)\, \delta_k$ to leading order in ϵ. Completing this derivation rigorously – including the definition of a well-posed Fourier-space measure factor consistent with diffeomorphism invariance, and verification that $\Xi_{\mu\nu}[\epsilon]$ vanishes as $\epsilon \to 0$ at the level of the full nonlinear field equations, not merely the weak-field limit – is identified in Sec. 9 as the principal remaining theoretical task of this research program.

B Numerical Pipeline: Additional Details

Table 2 lists the fiducial parameters used throughout Secs. 7–8. The linear growth ODE, Eq. (21), is integrated with `scipy.integrate.solve_ivp` (explicit RK45, relative tolerance 10^{-8}); the top-hat variance integrals for $\sigma(M)$ and σ_8 use adaptive Gauss–Kronrod quadrature (`scipy.integrate.quad`); the Limber integral, Eq. (38), is evaluated by direct trapezoidal quadrature over a χ-grid corresponding to $z \in [0, 3]$. All code is organized into the independently testable modules listed in Sec. 7.

Parameter	Fiducial value	Description
Ω_m	0.315	Matter density parameter (Planck 2018)
Ω_Λ	0.685	Dark-energy density parameter
h	0.674	Dimensionless Hubble parameter
n_s	0.965	Primordial spectral index
σ_8	0.811	ΛCDM normalization (used to fix SOC spectrum normalization)
ϵ_0	0.12	Fixed-point amplitude of the anomalous exponent
k_*	$0.35\, h\, \mathrm{Mpc}^{-1}$	Dimensional-flow transition scale
w	0.9	Transition width (in $\ln k$)

Table 2: Fiducial parameters used in the numerical pipeline of Sec. 7. The last three are illustrative choices (Sec. 9), not the result of a fit to data.

Acknowledgments

This Extended Version elaborates on the framework and phenomenology first outlined in the Condensed Version, Goldfain (2026), to which the reader is referred for a shorter, more compact presentation of the central hypothesis.

References

E. Goldfain, *From Self-Organized Criticality to Cosmological Anomalies (Condensed Version)*, companion preprint (2026).

Planck Collaboration, *Planck 2018 results. VI. Cosmological parameters*, Astron. Astrophys. **641**, A6 (2020).

S. Weinberg, *Cosmology*, Oxford University Press (2008).

S. Dodelson and F. Schmidt, *Modern Cosmology*, 2nd ed., Academic Press (2020).

V. Mukhanov, *Physical Foundations of Cosmology*, Cambridge University Press (2005).

P. J. E. Peebles, *Principles of Physical Cosmology*, Princeton University Press (1993).

P. J. E. Peebles, *The Large-Scale Structure of the Universe*, Princeton University Press (1980).

E. Kolb and M. Turner, *The Early Universe*, Addison-Wesley (1990).

J. M. Bardeen, *Gauge-invariant cosmological perturbations*, Phys. Rev. D **22**, 1882 (1980).

H. Kodama and M. Sasaki, *Cosmological perturbation theory*, Prog. Theor. Phys. Suppl. **78**, 1 (1984).

V. Mukhanov, H. Feldman, and R. Brandenberger, *Theory of cosmological perturbations*, Phys. Rept. **215**, 203 (1992).

W. Press and P. Schechter, *Formation of galaxies and clusters by self-similar gravitational condensation*, Astrophys. J. **187**, 425 (1974).

R. K. Sheth and G. Tormen, *Large-scale bias and the peak background split*, Mon. Not. R. Astron. Soc. **308**, 119 (1999).

R. K. Sheth and G. Tormen, *An excursion set model of hierarchical clustering*, Mon. Not. R. Astron. Soc. **329**, 61 (2002).

D. J. Eisenstein and W. Hu, *Baryonic features in the matter transfer function*, Astrophys. J. **496**, 605 (1998).

D. J. Eisenstein and W. Hu, *Power spectra for cold dark matter and its variants*, Astrophys. J. **511**, 5 (1999).

J. M. Bardeen, J. R. Bond, N. Kaiser, and A. S. Szalay, *The statistics of peaks of Gaussian random fields*, Astrophys. J. **304**, 15 (1986).

J. E. Gunn and J. R. Gott, *On the infall of matter into clusters*, Astrophys. J. **176**, 1 (1972).

Y. B. Zel'dovich, *Gravitational instability*, Astron. Astrophys. **5**, 84 (1970).

J. F. Navarro, C. S. Frenk, and S. D. M. White, *A universal density profile from hierarchical clustering*, Astrophys. J. **490**, 493 (1997).

W. J. G. de Blok, *The core-cusp problem*, Adv. Astron. **2010**, 789293 (2010).

A. Klypin, A. V. Kravtsov, O. Valenzuela, and F. Prada, *Where are the missing galactic satellites?*, Astrophys. J. **522**, 82 (1999).

B. Moore, S. Ghigna, F. Governato, et al., *Dark matter substructure within galactic halos*, Astrophys. J. **524**, L19 (1999).

M. Boylan-Kolchin, J. S. Bullock, and M. Kaplinghat, *Too big to fail? The puzzling darkness of massive Milky Way subhaloes*, Mon. Not. R. Astron. Soc. **415**, L40 (2011).

M. Milgrom, *A modification of the Newtonian dynamics as a possible alternative to the hidden mass hypothesis*, Astrophys. J. **270**, 365 (1983).

M. Bartelmann and P. Schneider, *Weak gravitational lensing*, Phys. Rept. **340**, 291 (2001).

P. Schneider, *Weak Gravitational Lensing*, Living Rev. Relativ. **9**, 1 (2006).

M. LoVerde and N. Afshordi, *Extended Limber approximation*, Phys. Rev. D **78**, 123506 (2008).

C. Heymans et al. (KiDS Collaboration), *KiDS-1000 cosmology: Multi-probe weak gravitational lensing and spectroscopic galaxy clustering constraints*, Astron. Astrophys. **646**, A140 (2021).

M. Asgari et al. (KiDS Collaboration), *KiDS-1000 cosmology: Cosmic shear constraints and comparison between two point statistics*, Astron. Astrophys. **645**, A104 (2021).

DES Collaboration, *Dark Energy Survey Year 3 results: Cosmological constraints from galaxy clustering and weak lensing*, Phys. Rev. D **105**, 023520 (2022).

D. Scolnic et al., *The Pantheon+ analysis: The full data set and light-curve release*, Astrophys. J. **938**, 113 (2022).

DESI Collaboration, *DESI 2024 VI: cosmological constraints from the measurements of baryon acoustic oscillations*, arXiv:2404.03002 (2024).

Euclid Collaboration, *Euclid preparation: Forecasts for redshift-space distortions*, Astron. Astrophys. (2024).

I. Labbé et al., *A population of red candidate massive galaxies* ~ 600 *Myr after the Big Bang*, Nature **616**, 266 (2023).

S. L. Finkelstein et al., *CEERS key paper. I. An early look into the first 500 Myr of galaxy formation with JWST*, Astrophys. J. Lett. **946**, L13 (2023).

R. P. Naidu et al., *Two remarkably luminous galaxy candidates at* $z \approx 10.5$–12.5 *revealed by JWST*, Astrophys. J. Lett. **940**, L14 (2022).

E. Bañados et al., *An 800-million-solar-mass black hole in a significantly neutral Universe at redshift 7.5*, Nature **553**, 473 (2018).

F. Wang et al., *A luminous quasar at redshift 7.642*, Astrophys. J. Lett. **907**, L1 (2021).

M. Boylan-Kolchin, *Stress testing* Λ*CDM with high-redshift galaxy candidates*, Nat. Astron. **7**, 731 (2023).

P. Bak, C. Tang, and K. Wiesenfeld, *Self-organized criticality: An explanation of* $1/f$ *noise*, Phys. Rev. Lett. **59**, 381 (1987).

P. Bak, C. Tang, and K. Wiesenfeld, *Self-organized criticality*, Phys. Rev. A **38**, 364 (1988).

M. J. Aschwanden et al., *25 years of self-organized criticality: Space and laboratory plasmas*, Space Sci. Rev. **198**, 47 (2016).

J. Ambjørn, J. Jurkiewicz, and R. Loll, *Reconstructing the Universe*, Phys. Rev. D **72**, 064014 (2005).

M. Reuter, *Nonperturbative evolution equation for quantum gravity*, Phys. Rev. D **57**, 971 (1998).

R. Percacci, *An Introduction to Covariant Quantum Gravity and Asymptotic Safety*, World Scientific (2017).

P. Hořava, *Quantum gravity at a Lifshitz point*, Phys. Rev. D **79**, 084008 (2009).

G. Calcagni, *Quantum field theory, gravity and cosmology in a fractal universe*, JHEP **03**, 120 (2010).

G. Calcagni, *Multifractional theories: an unconventional review*, JHEP **03**, 138 (2017).

B. Mandelbrot, *The Fractal Geometry of Nature*, Freeman (1982).

K. Falconer, *Fractal Geometry*, 3rd ed., Wiley (2014).

H. G. E. Hentschel and I. Procaccia, *The infinite number of generalized dimensions of fractals and strange attractors*, Physica D **8**, 435 (1983).

T. C. Halsey, M. H. Jensen, L. P. Kadanoff, I. Procaccia, and B. I. Shraiman, *Fractal measures and their singularities*, Phys. Rev. A **33**, 1141 (1986).

A. Rényi, *On measures of entropy and information*, Proc. Fourth Berkeley Symp. Math. Stat. Prob. (1961).

A. Rényi, *Probability Theory*, North-Holland (1970).

K. Wilson and J. Kogut, *The renormalization group and the ϵ expansion*, Phys. Rept. **12**, 75 (1974).

J. Cardy, *Scaling and Renormalization in Statistical Physics*, Cambridge University Press (1996).

Y. Kuramoto, *Chemical Oscillations, Waves, and Turbulence*, Springer (1984).

I. S. Aranson and L. Kramer, *The world of the complex Ginzburg-Landau equation*, Rev. Mod. Phys. **74**, 99 (2002).

J. Guckenheimer and P. Holmes, *Nonlinear Oscillations, Dynamical Systems, and Bifurcations of Vector Fields*, Springer (1983).

E. V. Linder, *Cosmic growth history and expansion history*, Phys. Rev. D **72**, 043529 (2005).

D. Foreman-Mackey, D. W. Hogg, D. Lang, and J. Goodman, *emcee: The MCMC hammer*, Publ. Astron. Soc. Pac. **125**, 306 (2013).

A. Lewis and S. Bridle, *Cosmological parameters from CMB and other data: A Monte Carlo approach*, Phys. Rev. D **66**, 103511 (2002).

A. Lewis, *Cobaya: Code for Bayesian analysis of hierarchical physical models*, arXiv:1910.13970 (2019).

W. H. Press, S. A. Teukolsky, W. T. Vetterling, and B. P. Flannery, *Numerical Recipes*, 3rd ed., Cambridge University Press (2007).

E. Hairer, S. P. Nørsett, and G. Wanner, *Solving Ordinary Differential Equations I*, Springer (1993).

E. Goldfain, *General Relativity from Primordial Dimensional Fluctuations*, Prespacetime J. (2021).

E. Goldfain, *Dimensional Regularization from Large Deviations Theory*, Prespacetime J. (2022).

E. Goldfain, *On Complex Dynamics and Standard Model Parameters*, Int. J. Mod. Phys. (2020).

E. Goldfain, *Emergence of Conserved Charges from the Dimensional Flow: An Alternative Model*, viXra preprint (2020).

E. Goldfain, *Can Standard Model Parameters Emerge from Spatiotemporal Chaos?*, J. Adv. Phys. (2019).

E. Goldfain, *From Complex Dynamics to Effective Field Theory*, Qeios preprint (2019).

E. Goldfain, *Energy Content of Dimensional Deviations*, ResearchGate preprint (2018).

E. Goldfain, *Criticality in continuous dimensions and cosmological perturbations*, Academia.edu preprint (2017).